Zitierweise: *Angew. Chem. Int. Ed.* **2025**, *64*, e202515719
doi.org/10.1002/anie.202515719

Batteries **Hot Paper**

Unveiling the Influence of Formation Voltage on Li-Rich Layered Oxide Cathode

Kang Zhang[+], Yichun Zheng[+], Jianhua Yin, Yawen Yan, Yilong Chen, Yuan Tian, Yizhen Huang, Lianpeng Li, Jiyuan Xue, Wen Jiao, Na Liu, Lirong Zheng, Huan Huang, Jing Zhang, Deniz Wong, Bodry Tegomo Chiogo, Christian Schulz, Yang Sun, Chongheng Shen,* Qingsong Wang,* Yu Qiao,* and Shi-Gang Sun*

Abstract: Lithium-rich layered oxide (LRLO) cathodes are recognized for their high energy densities, primarily driven by oxygen-related anionic redox activities, yet substantial activation of this process simultaneously induces structural instability. The typical voltage range in academic studies spans 2.0–4.8 V. Although 2.5–4.5 V are generally considered in industrial applications for enhanced capacity retention and electrolyte compatibility, this moderate voltage window leads to reduced capacity. To address energy density limitations, several top battery suppliers propose to separately increase the formation voltage during the initial cycle to enhance capacity, while other companies (e.g., Contemporary Amperex Technology Co., Ltd., CATL) claim that this high-voltage formation protocol would exacerbate cycling capacity fading. Herein, we systemically demonstrate that high-voltage formation promotes substantial Li^+ extraction from the transition metal (TM) layers, creating vacancies (in TM layer) that drive in-plane TM migration. This migration triggers a transformation in the OM_6 (M, cation) configuration from O4 (OLi_xTM_2) to O5 (OLi_yTM_1). Such evolution simultaneously enhances both anionic and cationic redox activity, collectively boosting capacity. Nonetheless, the induced in-plane TM migration would further aggravate out-of-plane TM migration, leading to progressive structural degradation, which has been elucidated as the main reason for cycling capacity fading.

Introduction

The increasing adoption of electric vehicles and the pressing need for advanced energy storage systems have intensified the demand for advanced lithium-ion batteries with ultrahigh energy density,[1–3] which rely heavily on cathodes.[4] Lithium-rich layered oxide (LRLO) cathodes have emerged as promising cathode materials for next-generation lithium-ion batteries due to their excellent energy density (>1000 Wh kg^{-1}), which is mainly attributed to the activation of oxygen-related anionic redox activities.[5–7] Nevertheless, the realization of the theoretical capacity advantage of LRLO requires operation at high voltage, which exposes critical challenges of electrolyte and structural stability.[8]

Recent research on the LRLO structure has predominantly focused on mitigating classic structural distortions, such as transition metal (TM) out-of-plane migration, oxygen loss, and voltage hysteresis.[9–11] These issues fundamentally arise from the extensive vacancy formation caused by the significant deintercalation of lithium ions from the TM layers, as well as the pronounced activation of anionic redox activity.[12] So far, the mechanisms underlying these problems

[*] K. Zhang[+], J. Yin, Y. Yan, Y. Chen, Y. Tian, Y. Huang, L. Li, J. Xue, Y. Qiao, S.-G. Sun
State Key Laboratory of Physical Chemistry of Solid Surfaces, Department of Chemistry, College of Chemistry and Chemical Engineering, Xiamen University, Xiamen 361005, P.R. China
E-mail: 36520211151887@stu.xmu.edu.cn
yuqiao@xmu.edu.cn

Y. Zheng[+], Y. Sun
School of Materials, Sun Yat-sen University, Shenzhen 518107, P.R. China

W. Jiao, N. Liu, C. Shen
Materials Innovation Department (MID), Contemporary Amperex Technology Co., Limited (CATL), Ningde 352100, P.R. China
E-mail: ShenCH@catl.com

L. Zheng, H. Huang, J. Zhang
Beijing Synchrotron Radiation Facility, Institute of High Energy Physics, Chinese Academy of Sciences, Beijing 100049, P.R. China

D. Wong, B. T. Chiogo, C. Schulz
Helmholtz-Center Berlin for Materials and Energy, Hahn-Meitner-Platz 1, Berlin 14109, Germany

Q. Wang
Bavarian Center for Battery Technology, Department of Chemistry, University of Bayreuth, Bayreuth 95447, Germany
E-mail: qingsong.wang@uni-bayreuth.de

[+] Both authors contributed equally to this work.

Additional supporting information can be found online in the Supporting Information section

in LRLO have been to some extent well elucidated. From a structural chemistry perspective, improving these issues through doping at specific sites is well-defined,[13–15] and the approach for introducing the relevant elements into the appropriate sites is clear within materials science.[16–18] Nevertheless, the current focus is on a challenge that is most closely associated with practical applications, the balancing of working voltage and formation voltage, which is also the critical issue for the industrialization of LRLO.

Academic research (dominated in published papers) typically employs cycling protocols within the voltage range of 2.0–4.8 V, while the industrial implementation of these high-voltage regimes remains impeded by accelerated capacity fading and safety concerns. In contemporary industrial practice, as exemplified by the operational protocols of several top battery suppliers, cycling of LRLO cathodes is typically confined to the charge cut-off voltage around 4.5 V. While this moderate voltage window delivers reduced specific capacity compared to the 4.8 V high-voltage regime, it substantially enhances cycling stability and maintains compatibility with established high-voltage electrolyte (e.g., formulations designed for mid-nickel cathode systems NCM622). This strategic voltage limitation not only reduces gas evolution but also enhances thermal safety, both of which are critical factors for commercial/practical viability.

Nevertheless, the persistent industrial demand for higher energy densities has driven the exploration of pre-activation methods through increasing the formation voltage, aiming to maximize capacity within the moderate operating voltage window (e.g., within 2.5–4.5 V working voltage region). This phenomenon is unique to LRLO, distinguishing it from conventional layered oxide cathodes such as $Ni_xCo_yMn_zO_2$ and $LiCoO_2$. Therefore, critical issues remain within the scientific community regarding the impact of such pre-activation protocols of LRLO, particularly concerning dynamic structural transformations during electrochemical conditioning and interfacial reactivity at extreme voltages. These directly hinder the reliable assessment of material stability and the optimization of the electrolyte.

In this study, we collaborated with Contemporary Amperex Technology Co. Limited (CATL) to systematically investigate the impact of formation voltage on LRLO. By elevating the initial formation voltage from 4.5 to 4.8 V (versus Li^+/Li) while maintaining subsequent cycling within 2.5–4.5 V, we observed a 37 mAh g^{-1} increase in the second discharge capacity. However, this improvement coincides with accelerated long-term capacity fading. Multimodal characterizations reveal that high-voltage formation promotes the Li^+ deintercalation from the TM layer, triggering an increase in TM layer vacancies. This facilitates in-plane TM migration and drives a transformation in the OM_6 (M, cation) configuration from O4 (OLi_xTM_2) to O5 (OLi_yTM_1). This structural evolution simultaneously enhances the anionic/cationic redox activity, collectively improving the overall capacity. Crucially, the induced in-plane TM migration further aggravates out-of-plane TM migration, culminating in progressive structural degradation. These successive structural degradations are identified as the primary cause of the observed capacity retention loss under high-voltage formation conditions. Notably, interfacial degradation exhibits a negligible impact on capacity retention, suggesting that bulk structural evolution rather than surface effects dominates the capacity degradation.

Results and Discussion

Trade-Off Between Capacity and Cycle Life Derived by Formation Voltage

In the current lithium-ion battery systems, the oxidation decomposition threshold of commercial carbonate-based electrolytes (typically composed of EC/EMC/$LiPF_6$) is strictly confined within the range of 4.3 to 4.5 V (versus Li^+/Li).[19] To ensure the safety and stability of the battery system, the practical operating voltage of lithium-rich layered oxide (LRLO) materials is typically limited to below 4.5 V. However, this voltage constraint restricts the utilization of the high capacity enabled by anion redox reactions (ARR), resulting in around 60%–70% of its theoretical value (> 300 mAh g^{-1}) being achieved, as illustrated in Figure S1. Therefore, while maintaining the stability of the electrolyte, how to maximize the anion redox activity of LRLO has become a key technical challenge in its industrialization process. Based on the synthesized $Li_{1.14}Ni_{0.26}Mn_{0.55}Co_{0.05}O_2$ (with morphological characteristics as shown in Figure S2, this study designed a gradient voltage activation protocol.

Four distinct formation voltage protocols of 4.5, 4.55, 4.65, and 4.8 V (activation for 1 cycle), and consistently maintaining the cycling range of 2.5–4.5 V over 200 cycles for long-term performance tests. Figure 1a illustrates the long-cycle charge-discharge profiles of LRLO in different formation voltages during the first 200 cycles, along with the capacity decay rate from 50 to 200 cycles. As the formation voltage increased gradually from 4.5 to 4.8 V, the subsequent discharge capacity exhibited a progressive increase, which confirms that high-voltage formation (HVF, 4.8 V) significantly enhances the anion/cation redox capability in comparison to low-voltage formation (LVF, 4.5 V). However, this capacity enhancement is accompanied by a general degradation in cycling stability. Considering the capacity activation process in the initial tens of cycles (as shown in Figure S3), the capacity from cycles 50 to 200 was selected to compare the capacity decay rate. As the formation voltage increased, the decay angle rose from 29° to 36°, indicating that HVF accelerates the capacity decay over extended cycling of LRLO. As depicted in Figure 1b, when the formation voltage increased from 4.5 to 4.8 V, the discharge capacity in the second cycle significantly increased by 21.6% (from 172.46 to 209.78 mAh g^{-1}), but the capacity retention at the 200th cycle (versus 5th cycle, which is considering the significant capacity fluctuations in the first four cycles) decreased by 15.8% (from 94.92% to 79.14%).

This inversion of voltage-dependent performance is primarily attributed to the change of the dynamic balance between anion redox activation and structural stability. Notably, there is an ongoing debate (as shown in Figure 1c) regarding the capacity decay mechanism induced by HVF: 1) From the cathode department: the interface dominance theory posits that continuous oxidative decomposition of the

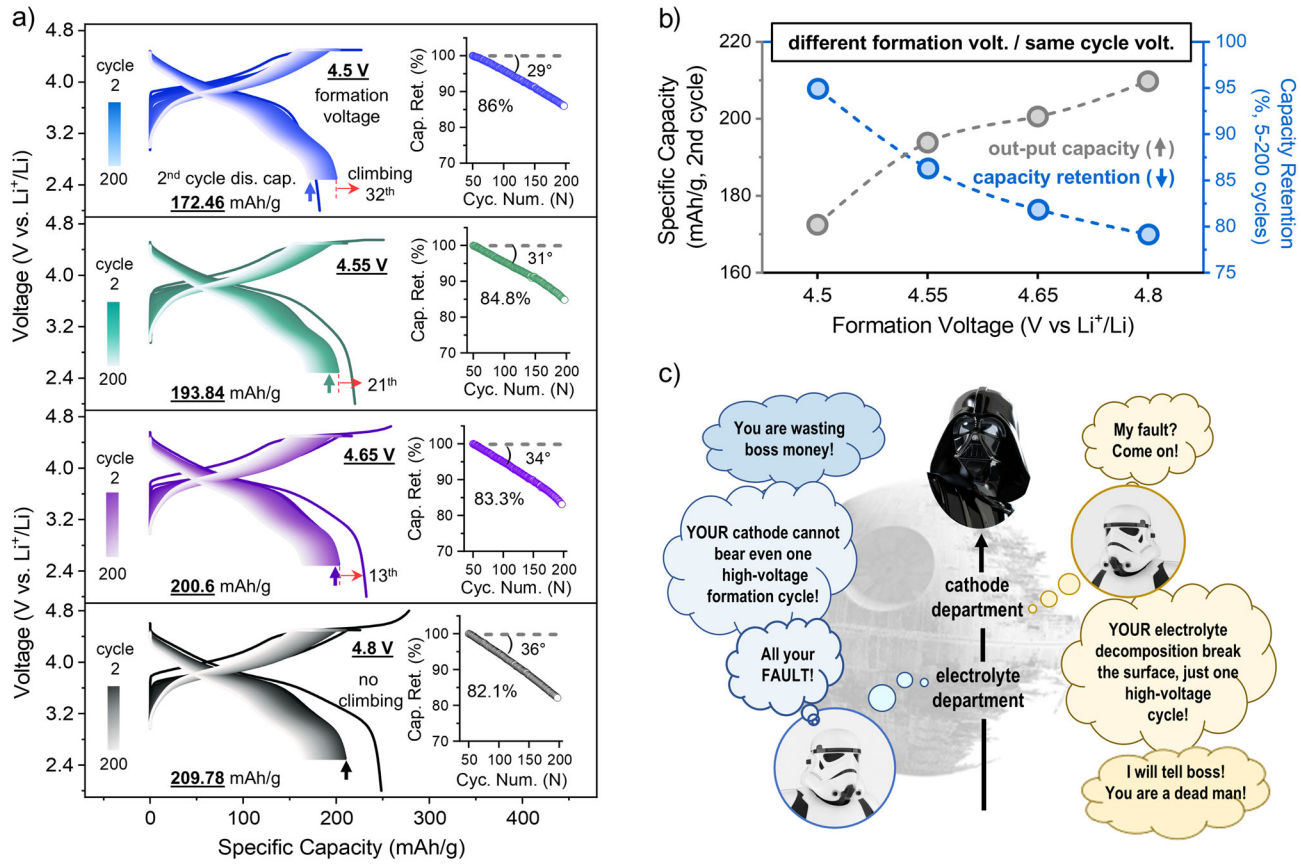

Figure 1. Electrochemical performance distinctions of LRLO in different formation voltages. a) The long-cycle charge–discharge curves of LRLO for Li half-cell after forming at 4.5, 4.55, 4.65, and 4.8 V, respectively. Inset: capacity retention from 50 to 200 cycles. The blue, green, purple, and black arrows indicate the discharge capacity for the second cycle. The red arrow indicates the number of cycles when the capacity climbing reaches its maximum value. b) Discharge capacity of the second cycle and capacity retention from 5 to 200 cycles for Li half-cell at different formation voltages. c) Cartoon diagram of the controversy over high-voltage formation protocol (Reproduced with permission).

electrolyte at voltages above 4.8 V (EC/EMC oxidizing to CO_2) leads to a significant increase in interface impedance and the degradation of cathode active materials; 2) From the electrolyte department: the bulk dominance theory suggests that phase transitions and/or other voltage structural distortion driven by the migration of transition metals (TM), from layered to spinel and rock salt phases, impede Li^+ transport pathways, which finally lead to poor cycle life with HVF. The crux of this debate lies in the precise elucidation of the underlying mechanisms governing capacity degradation under HVF protocols, thereby guiding the optimization of lithium-rich cathode charging protocols. Given that the high capacity of LRLO from 4.5 to 4.8 V is primarily driven by the ARR, the degradation of long-cycle performance under HVF is undoubtedly linked to the activation of this high capacity. However, the underlying mechanism remains poorly understood.

Cationic/Anionic Charge Compensation Mechanism During HVF and LVF

To investigate the electrochemical activation mechanism of LRLO within the 2.5–4.5 V cycling window, this study employs dynamic voltage scanning coupled with dQ/dV analysis. As shown in Figure 2a on the left side, when charging exceeds 4.1 V (red curve), the discharge curve exhibits a distinct voltage hysteresis in the 2.8–3.5 V range, which is primarily attributed to the asymmetric redox mechanism of oxygen-related anions.[20–22] The dQ/dV curve presented on the right side of Figure 2a illustrates the attribution of different redox peaks. The redox peaks within the blue region (2.5–3.5 V) are primarily associated with the synergistic reduction of Mn^{3+}/Mn^{4+} and O^{2-}/O^{n-} ($n > -2$), while the green region (3.5–4.1 V) corresponds mainly to the charge compensation mechanisms of Ni^{2+}/Ni^{3+}, Mn^{3+}/Mn^{4+}, and O^{2-}/O^{n-}.[23] The red region (4.1–4.5 V) is predominantly linked to the strong coupling mechanism between the Ni^{3+}/Ni^{4+} and the O^{2-}/O^{n-} redox processes. Figure 2b shows the discharge dQ/dV curves for the second cycle at different formation voltages. Compared to LVF, HVF significantly enhanced the intensity of the redox peaks in all regions, suggesting a substantial activation of the multi-element (Mn/Ni/O) cooperative charge compensation mechanism. However, the specific charge compensation mechanism of HVF needs to be further elucidated.

To elucidate the influence of formation voltage on the charge compensation mechanism of LRLO, a comparative

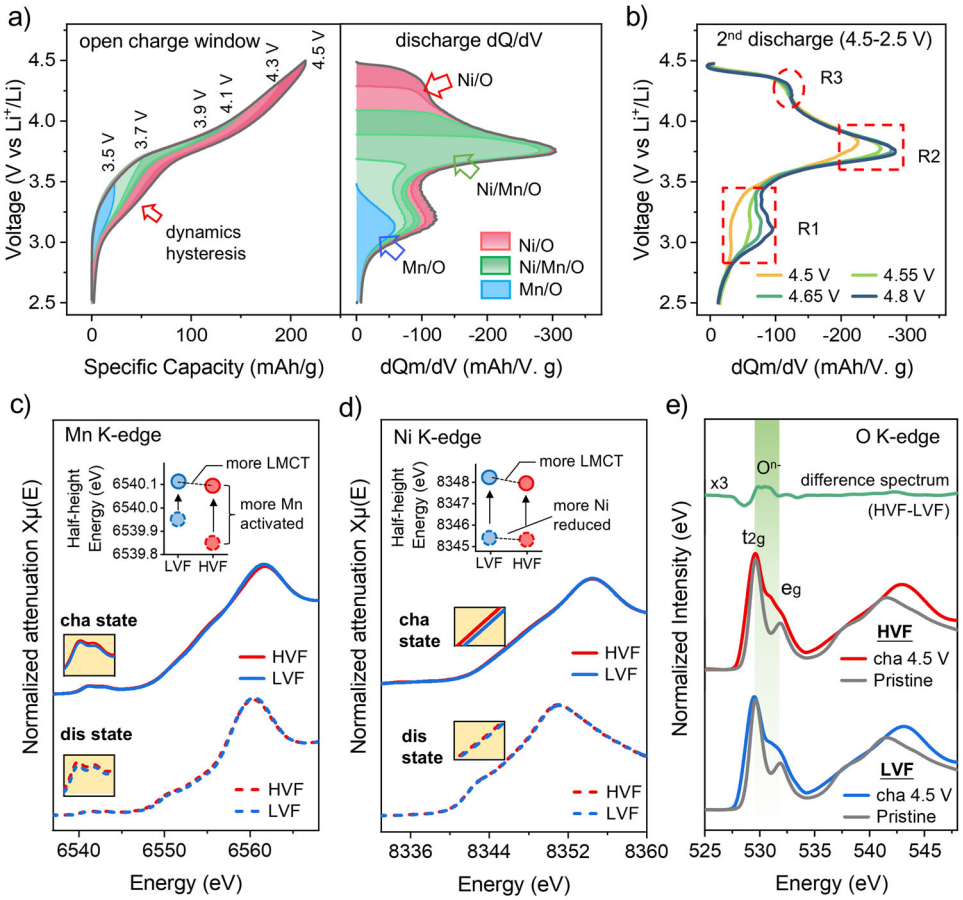

Figure 2. Cationic/anionic charge compensation mechanism. a) Voltage profiles and corresponding d*Q*/d*V* curves in Li half-cells as the charge window is opened stepwise from 2.5 to 4.5 V. b) The d*Q*m/d*V* curves of the second cycle in different formation voltages. c) Evolution of normalized XANES spectra of Mn K-edge and d) Ni K-edge of LRLO during the 2nd charge–discharge process after HVF and LVF. Inset: Half-height changes during in operando XANES at the Mn and Ni K-edge. e) O K-edge s XAS spectra collected at pristine and charged to the same 4.5 V for HVF and LVF. Inset: the difference spectrum is shown inset for clarity.

experiment was conducted using 4.5 and 4.8 V as the LVF and HVF. The evolution of the electronic structure of TM during the charge-discharge process (2.5/4.5 V) was examined through X-ray absorption spectroscopy (XAS). Typically, the first two pre-edge absorption (~6539 and ~6545 eV, as shown in the inset) correspond to the transitions from 1s to $3d_{eg}$ and $3d_{t2g}$. which are caused by the pure electric quadrupole coupling and/or the 3d–4p orbital mixing arising from the noncentrosymmetric environment of the slightly distorted octahedral 3a sites in rhombohedral R-3m space group[24] The increased intensity of the Mn K-edge XANES pre-edge feature reflects an irreversible transition of the Mn local coordination environment from a high-symmetry octahedral structure to a low-symmetry tetrahedral configuration. This symmetry-breaking phenomenon is closely linked to the TM in-plane/out-of-plane migration. Due to the difficulty in directly distinguishing the valence state changes of Mn from the Mn K-edge data, the half-height position of the lower energy peak was used as an indicator for the Mn K-edge (inset in Figure 2c).[25–27] As illustrated in Figure 2c, under the same charge state (4.5 V), the LRLO cathode subjected to HVF exhibited a slight decrease in half-height energy, which can be attributed to the charge transfer from ligands (O) to metal (Mn) process (LMCT). Conversely, at the same discharge state (2.5 V), HVF demonstrated a significant decrease in half-height energy, indicating a deeper involvement of Mn in charge compensation during the discharge process.[28] We performed a statistical analysis of the energy shifts during the charging and discharging states under both HVF and LVF, as presented in Figure 2c (inserted figure). The larger half-height energy shift observed during charge–discharge in HVF suggests a greater activation of Mn, thereby enhancing its involvement in charge compensation. On the other hand, at the Ni K-edge, HVF exhibited a lower half-height energy compared to LVF at the same charging state (Figure 2d), which can be attributed to a greater charge transfer from ligands (O) to metal (Ni) in the former.[29–31] At the same discharging state, HVF showed a slight decrease in edge energy of Ni, suggesting that HVF facilitates the activation of more Ni for participation in charge compensation during the discharge process.

To investigate the regulatory mechanisms by which different formation voltages influence lattice oxygen activity, we utilized soft X-ray absorption spectroscopy in total electron

yield mode (TEY-sXAS) to examine the electronic structure at the O K-edge. The initial region of the O K-edge absorption spectrum (~528 eV) corresponds to the transition of O 1s electrons to the empty hybridized orbitals of TM 3d-O 2p, with the t_{2g} orbitals exhibiting weaker hybridization compared to the e_g orbitals.[32] The intensity variation of the characteristic peak at ~531 eV serves as a direct indicator of the activation extent of reversible oxygen redox processes. As shown in Figure 2e, under identical charging conditions, samples subjected to HVF exhibit a markedly increased electron unoccupied states at 4.5 V, corresponding to anion oxidation. This difference in activation degree can be distinctly observed through differential spectroscopy analysis, suggesting that HVF substantially promotes the depth of lattice oxygen involvement in charge compensation. Additionally, the O^{n-} species charged to 4.5 V after HVF and LVF for the second cycle were further quantitatively analyzed through the titration mass spectroscopy (TMS) method,[33] which suggests that a large amount of O^{n-} is activated after HVF (Figure S4). From the perspective of charge compensation mechanisms, it is evident that the synergistic enhancement of anion/cation redox activity induced by HVF is closely associated with the reconstruction of the local coordination environment resulting from TM migration.

The Influence of OM_6 (M, cation) Configuration Evolution Under HVF and LVF

To elucidate the structural evolution of LRLO under voltage modulation, we employed high-resolution resonant inelastic X-ray scattering (RIXS) to monitor the dynamic evolution of oxygen species during the first charging cycle. The intensity changes in the vibrational peaks near the elastic signal at 0 eV and a distinct energy loss at ~8 eV are two main features associated with O─O dimer.[34–37] As illustrated in Figure 3a, increasing the charging voltage from 4.5 to 4.8 V led to a consistent enhancement in the intensity of the vibrational peaks at the 0.125–2.2 eV region, a trend that is clearly evident in the inset. This change suggests a continuous increase in O─O dimers as the charging voltage rises. Typically, increased O─O dimer signals are indicative of an increase in the aggregation of vacancies within the cathode material,[35,38] implying that HVF may accelerate the migration of TM and promote the formation of aggregated vacancies. This is consistent with the significant increase in the intensity of the pre-edge peak of the Mn K-edge XANES after HVF in the same charge/discharge state shown in Figure 2c, suggesting a more pronounced irreversible transformation of the Mn coordination environment from an octahedral to a tetrahedral structure.[39,40] Furthermore, the migration energy barrier of Mn was calculated using the nudged elastic band (NEB) method at formation voltages of 4.5 and 4.8 V. As shown in Figure S5, a lower migration energy barrier is observed at 4.8 V, confirming that more pronounced TM migration and vacancy aggregation occur under 4.8 V. These computational results are in excellent agreement with the trends identified by RIXS. As depicted in Figure 3b, the dynamic process of coordination reconfiguration in the LRLO under voltage modulation was elucidated based on the RIXS and NEB results. In the pristine material, lithium ions were arranged in a superlattice structure within the TM layer, with O coordinated to a TM_2Li_4 environment (O4 configuration, represented by purple spheres, as shown in the upper-left model of Figure 3b). Upon charging to 4.5 V, Li^+ increasingly migrated out of the TM layer, leading to the formation of separated lithium vacancies and concomitant oxidation of the O atoms. A slight TM in-plane migration led to a partial transformation of the O coordination environment to a TM_1Li_5 configuration (O5 configuration, represented by yellow spheres), corresponding to the O─O dimer signal observed in the RIXS spectrum at 4.5 V (Figure 3a). As the voltage was further increased to 4.8 V, the extensive removal of Li^+ and continued oxidation of oxygen initiated large-scale cation migration within the TM layer, thereby facilitating a significant increase in O─O dimer formation, consistent with the enhanced O─O dimer signal detected at the 4.8 V charging state in Figure 3a. However, the extensive formation of aggregated vacancies was accompanied by a continuous transformation in the O coordination environment, with the O4 coordination configuration gradually decreasing and the O5 configuration increasing. DFT-based on the special quasi-random structures (SQS) simulations (Figures S6a and 6b) indicates that the proportion of O4 coordination decreases progressively with increasing charging voltage, from nearly complete occupancy in the pristine state to ~90% at 4.5 V and further down to ~80% at 4.8 V. Notably, during the discharge process back to 2.0 V, the Li^+ reinsert into TM layer. However, the O coordination environment exhibited irreversible behavior, which resulted in the persistent accumulation of the O5 configuration throughout the cycling process. As illustrated in Figure 3c, at the same charging state of 4.5 V, compared with LVF, the integral intensity of the O─O dimer characteristic peak in the 0.125–2.2 eV range significantly increased by 29.7% for HVF, suggesting that the HVF facilitated the formation of a denser vacancy aggregation. This phenomenon of vacancy aggregation is closely associated with the irreversible transformation of the O coordination environment from O4 to O5.

First-principles calculations were used to systematically investigate the regulatory mechanisms by which the O4 and O5 coordination configurations influence the redox activity of anions (Figure 3d,f). Density of states (DOS) analysis indicated that the O5 configuration exhibited a more significant distribution of non-bonding orbital electronic states near the Fermi level (from −2 to 0 eV), with the ratio of non-bonding state density between O5 and O4 being 1.6:1. This behavior can be attributed to the presence of a single non-bonding orbital in the O4 configuration and two non-bonding orbitals in the O5 configuration.[41] It is noteworthy that the O5 coordination configuration (Figure 3f) exhibits a higher top energy band (U_{2p}) compared to the O4 configuration (Figure 3e), suggesting that the O5 configuration facilitates the formation of electron holes in the O_{2p} band and promotes the oxidation of lattice oxygen. This, in turn, enhances redox activity and improves charge compensation. The evolution of the electronic structure is attributed to the induced effects resulting from changes in the coordination environment:

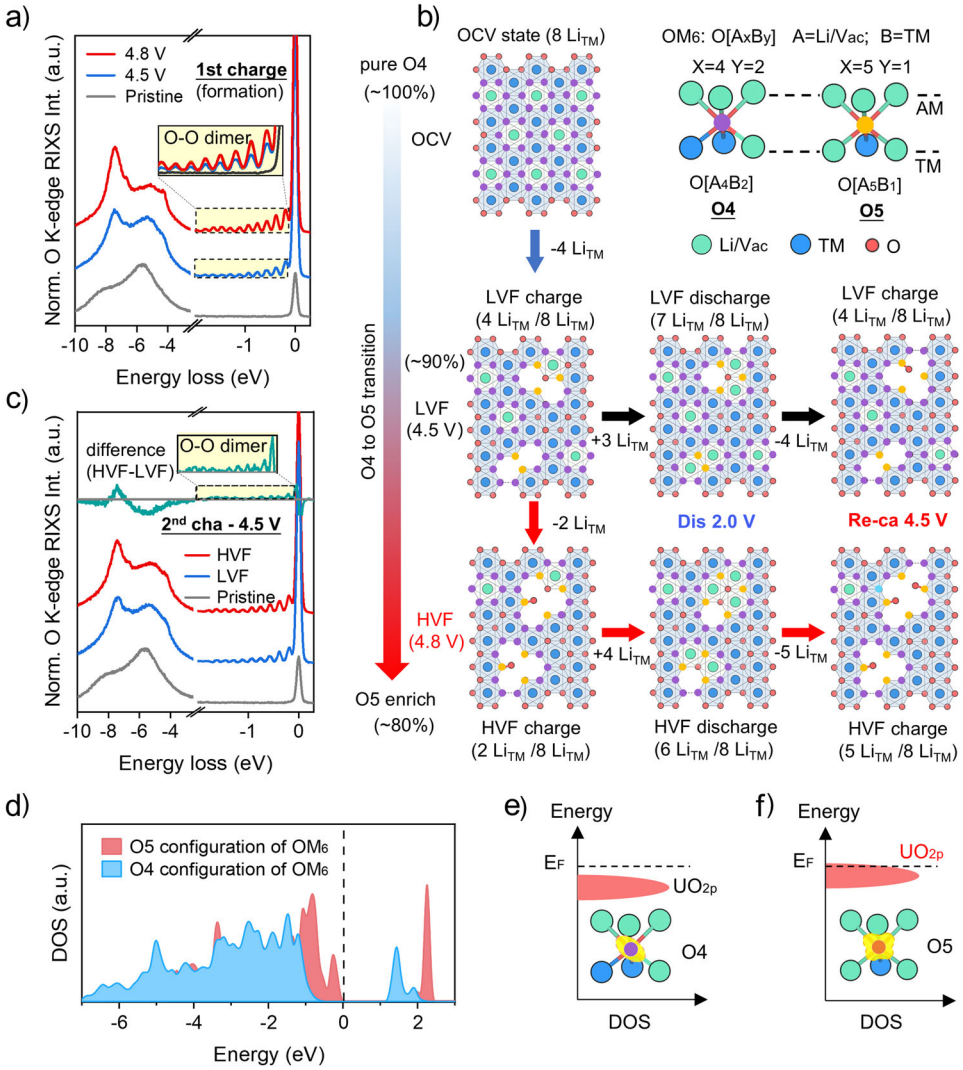

Figure 3. The influence of OM_6 configuration evolution under HVF and LVF. a) High-resolution RIXS spectra recorded at an excitation energy of 531 eV for LRLO in the pristine, charged to 4.5 V and charged to 4.8 V during the initial charge process. Inset: enlarged region from 0.125–2 eV. b) High-resolution RIXS spectra recorded at an excitation energy of 531 eV for LRLO in the pristine and charged to the same 4.5 V for the 2nd cycle in HVF and LVF. Inset: enlarged region from 0.125–2 eV region and the difference spectra are shown for clarity. c). The formation and evolution schematic illustrations of clusters during HVF and LVF. Color-coding in insets is the same as the other structural figures: green, Li; red, O (purple: O4; yellow: O5); blue, TM. The red arrow signifies HVF and the black arrow signifies LVF. d) The PDOS of the O4 and O5 2p orbitals in pristine. Schematic diagram of the UO_{2p} band structure of O4 e) and O5. f). The yellow area indicates the charge density.

when a positively electronegative M atom replaces a partially negatively electronegative TM atom, a competitive covalent bonding mechanism between TM─O and M─O is established, driving electron redistribution toward the atom with higher electronegativity (as depicted in Figures S7a and S7b). Consequently, the atomic orbital overlap between the TM and O is enhanced, which lowers the energy of the bonding molecular orbitals and increases the energy of the anti-bonding molecular orbitals (Figure S8). This, in turn, strengthens the covalency of the TM─O bond and lowers the redox potential, which is supported by the LOBSTER-based crystal orbital Hamiltonian population (COHP) calculations and the corresponding integrated COHP (ICOHP) values shown in Figure S9 (the −ICOHP value for the O5─TM bond is 3.31 eV while the O4─TM bond is 2.48 eV).[42,43] Particularly significant is the activation of the ligand–metal charge transfer (LMCT) mechanism by the O5 configuration, which aligns with experimental observations of a reduced Mn and Ni oxidation state in the charged state (Figure 2c,d). The O5 configuration, formed HVF, significantly strengthens the TM─O covalency, optimizes the charge compensation pathways between anions and cations, and thereby enhances the capacity in subsequent cycles. However, this also introduces challenges related to the structural stability of the material.

In-Plane/Out-Of-Plane TM Migration During Subsequent Cycle

The transformation of the O4 to O5 coordination configuration induced by HVF is accompanied by the

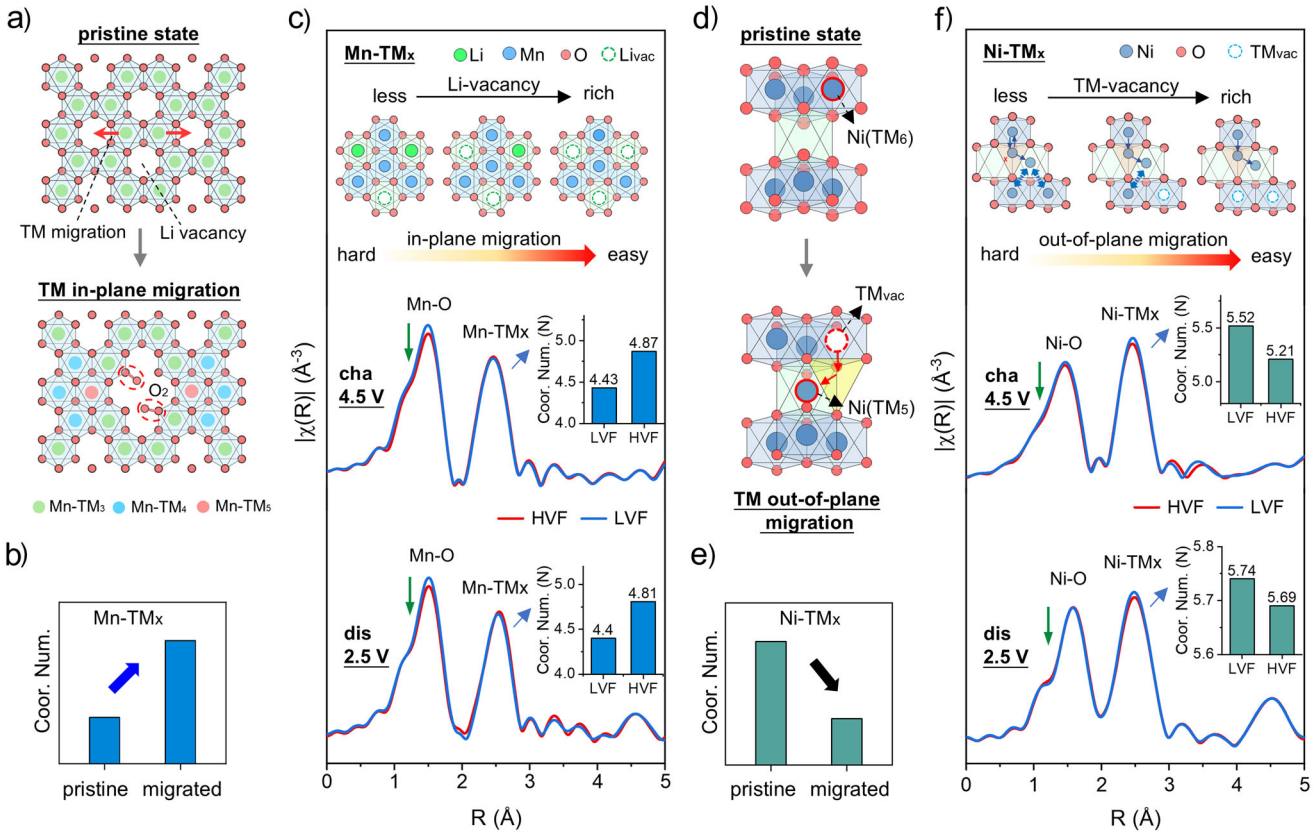

Figure 4. Transition metal in-plane/out-of-plane migration. a) A schematic model illustrating coordination changes induced by the in-plane TM migration in the TM layer. Green, blue, and red spheres denote Mn–Mn_3, Mn–Mn_4, and Mn–Mn_5 configurations, respectively. The red arrow indicates the migration path of TM. b) The coordination changes before and after migrating. c) The EXAFS spectra of Mn and the intensity variations of Mn–TM under the same charge and discharge states under HVF and LVF. Inset: Mn–TM coordination and in-plane migration from easy to hard. d) A schematic model illustrating coordination changes induced by the TM out-of-plane migration. e) The coordination changes before and after migrating. f) The EXAFS spectra of Ni and the intensity variations of Ni–TM under the same charge and discharge states under HVF and LVF. Inset: Ni–TM coordination and out-of-plane migration from easy to hard.

three-dimensional migration of TM, revealing the atomic-scale structural dynamics of LRLO. As shown in Figure 4a, a simplified model is employed to illustrate the interrelationship between in-plane TM migration within the TM layer and changes in coordination number. In the original $LiTM_6$ superlattice, the TM (primarily Mn) are arranged in a honeycomb pattern (TM–TM_3). During the charging process, the proliferation of lithium vacancies triggers in-plane migration within the TM layer, causing a transition from TM–TM_3 to TM–$TM_{4/5/6}$, which results in an increase in coordination number (Figure 4b).

This means that the extent of in-plane migration within the TM layer and the degree of vacancy aggregation can be inferred from the variation in the Mn–TM coordination number. During the charging process, as the concentration of Li vacancies within the TM layer increases, the migration pathways of the TM become more numerous, which is conducive to the in-plane TM migration (as depicted in the inset, where red represents O, blue represents Mn, green represents Li, and the dashed line denotes Li vacancies). Extended X-ray absorption fine structure (EXAFS) analysis reveals that HVF protocol results in a reduced Mn—O peak intensity (the EXAFS fitting details are provided in Table S1) during both the charging and discharging states, which is primarily attributed to the more significant O-loss, coupled with the Mn migration from octahedron to tetrahedron, along with a reduction in central symmetry (e.g., Jahn–Teller distortion, as depicted in Figure S10). Additionally, the second shell of Mn K-edge EXAFS spectra is identified as Mn–TM interactions,[44] and the intensity increases for HVF, indicating a more significant in-plane migration within the TM layer and an increased degree of vacancy aggregation (inset Mn—O and Mn–TM coordination number change and the EXAFS fitting details are provided in Figure S11 and Table S2).

In the pristine $LiTMO_2$-like structure, the TM is coordinated to six neighboring TM atoms. During out-of-plane migration, the coordination shifts from TM–TM_6 to TM–TM_5, leading to a reduction in the coordination number (Figure 4d,e). As Ni atoms are predominantly located in the $LiTMO_2$ region, changes in the Ni coordination number serve as an indicator of TM out-of-plane migration. In the fully ordered crystal structure, the strong electrostatic repulsion between the TM layers creates a high-energy barrier that effectively impedes out-of-plane migration. However, as the aggregation of Li vacancies in the TM layer increases, the electrostatic repulsion between layers diminishes, thereby

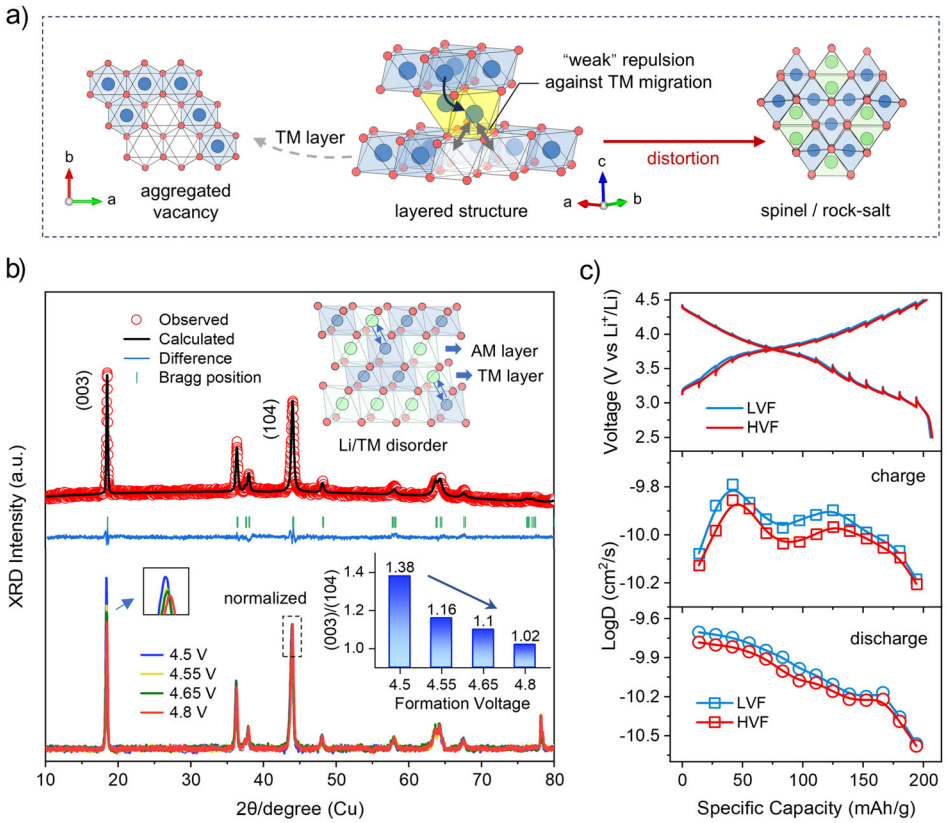

Figure 5. Stability of layered structure upon cycling. a) A schematic model illustrating phase changes from layered to spinel/rock salt. b) Ex situ XRD patterns and refined results of different formation voltages after 200 cycles. Insets present the peak intensity ratio of (003)/(104) and the enlarged view of the (003) crystal plane. c) GITT voltage curve and chemical diffusion coefficient [log(D_{Li+})] of HVF and LVF cycling after 100 cycles.

facilitating TM out-of-plane migration. EXAFS analysis of Ni reveals that, under both charging and discharging states, HVF results in a reduced Ni–TM peak intensity, suggesting enhanced TM out-of-plane migration (inset Ni–TM and Ni–O coordination number change and the EXAFS fitting details are provided in Figure S12 and Table S2). Under HVF protocol, the intense in-plane and out-of-plane TM migration not only disrupts the local coordination environment but also significantly affects the long-range order of the cathode material.

Stability of Layered Structure Upon Cycling

The in-plane TM migration of local structure intensifies out-of-plane migration, which is a distinctive characteristic unique to LRLO. As shown in Figure 5a, the enhanced in-plane TM migration produces vacancy aggregation within the TM layers, which in turn diminishes the electrostatic repulsion against migrated TM, aggravating out-of-plane TM migration. This severe out-of-plane migration subsequently induces a phase transformation from ordered layered structures to disordered spinel and rock-salt configurations. The cascade of TM migration processes ultimately accelerates the structural integrity degradation of LRLO.

Through the combined analysis of ex situ X-ray diffraction (XRD) and galvanostatic intermittent titration technique (GITT), this study unveils the profound impact of HVF on the long-range structural stability of LRLO. As shown in Figure 5b, the refinement results (Figure S13 and Table S3) indicate that after 200 cycles at different formation voltages, the cathode maintains R-3m layered structure. Notably, a significant change in the intensity ratio of the (003) and (104) peaks was observed, which can be attributed to Li/Ni cation mixing. The (003) plane is predominantly occupied by TM ions, while both Li and TM ions are distributed across the (104) plane. When TM ions migrate from the (003) plane to the (104) plane, the overall atomic scattering power of the (104) plane increases, which reduces the X-ray response from the (003) plane.[45] This results in an enhancement of the (104) diffraction peak intensity and a decrease in the (003) diffraction peak intensity (inset the schematic diagram of Li/Ni disorder). This behavior provides a basis for using the intensity ratio of the (003) and (104) peaks as an indicator of the degree of cation mixing. As shown in Figure 5b, with the formation voltage increasing from 4.5 to 4.8 V, the intensity ratio of the (003) to (104) peaks decreased by 35%, indicating that HVF significantly exacerbates ionic disorder and long-range structural degradation. However, high levels of Li/Ni cation mixing significantly hinder the Li^+ (de-)intercalation within the TM and alkali metal (AM) layers, markedly suppressing migration dynamics. Furthermore, through GITT, the dynamic differences between HVF and LVF were analyzed. Figure 5c displays the GITT voltage

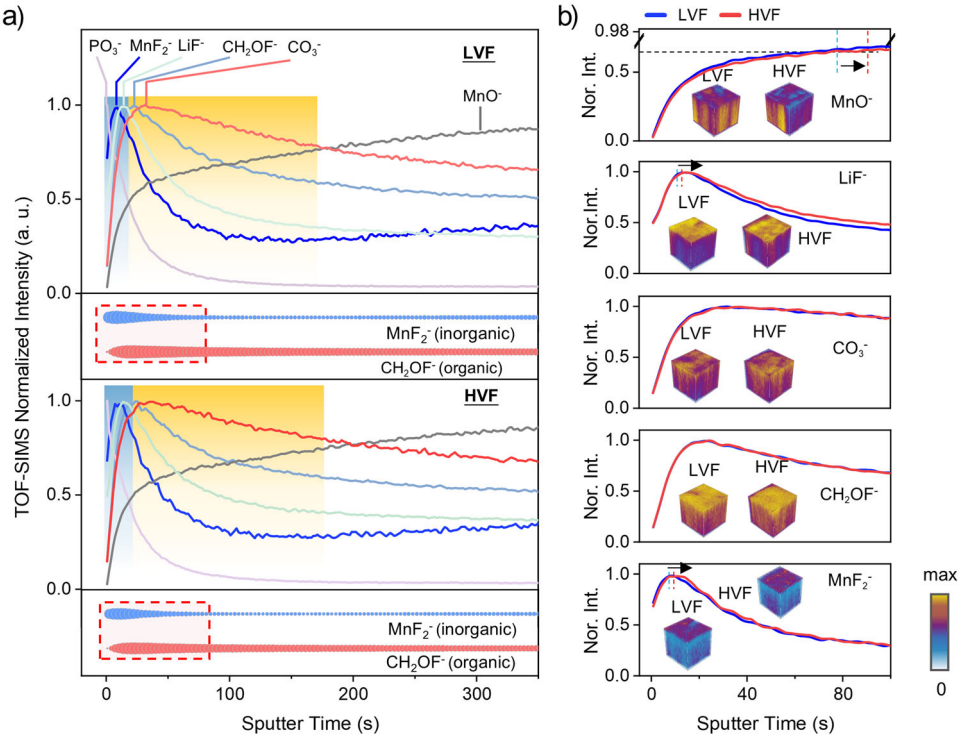

Figure 6. Interfacial stability of the cathode after LVF and HVF. a) TOF-SIMS characterization of the LRLO cathode electrodes after LVF and HVF. Normalized depth profiles of the interface and bulk fragments illustrate the structure of the CEI. b) The distribution depth of MnO^-, LiF^-, CO_3^-, CH_2OF^-, MnF_2^- in HVF and LVF are shown in partially enlarged drawings. The 3D renderings of selected secondary ion fragments from the cathode electrode. The sputtered volume is 100 μm (length) × 100 μm (width) × 150 nm (height).

profiles during charging and discharging after 100 cycles, along with the corresponding variations in Li^+ diffusion coefficients (D_{Li+}). The results show that, across the entire charge–discharge range, HVF exhibits a lower D_{Li+}, with this dynamic degradation attributed to more pronounced in-plane and out-of-plane TM migration under HVF, which hinders the diffusion of Li^+ within the material.

Assessment of Interfacial Stability After LVF/HVF

Although we have confirmed the distortion of the cathode structure at the structural level (such as the evolution of local covalent environment, the TM migration, and lattice distortion, etc.), several critical issues remain to be further verified. As suggested by the electrolyte department, the material structure is not as flawless as claimed by the cathode department. However, the hypothesis proposed by the cathode department regarding the voltage failure of electrolyte stability under HVF cannot be entirely ruled out. In other words, both factors may have contributed. As such, we are tasked with conducting a comprehensive study on the interface stability under both LVF and HVF.

To investigate the impact of different formation voltages on the cathode interface, coin cells (versus Li^+/Li) subjected to both HVF and LVF were disassembled. The depth and distribution of the electrolyte/cathode interface (CEI) film were then analyzed using time-of-flight secondary ion mass spectrometry (TOF-SIMS). Figure 6a displays the normalized TOF-SIMS depth profiles of selected secondary ions after HVF and LVF for the LRLO cathode CEI. In this analysis, MnO^- corresponds to the primary component of the cathode material, while PO_3^- and LiF^- are the decomposition products of $LiPF_6$, CO_3^-, and CH_2OF^- represent the degradation products of carbonate-based solvents, and MnF_2^- indicates the fluorinated transition metal species derived from the cathode active material.[46,47] The CEI thickness is defined as the point where the MnO^- intensity reaches 70% of its maximum value. The in-depth analysis of the normalized depth profiles indicates that both HVF and LVF samples exhibit a double-layer CEI structure. The outer layer is primarily composed of inorganic products, such as PO_3^-, MnF_2^-, and LiF^-, while the inner layer consists of organic decomposition products, including CH_2OF^- and CO_3^-. To facilitate a clearer comparison of the secondary ion depth distributions under HVF and LVF conditions, the etching curves of selected secondary ions were overlaid (Figure 6b). Comparative analysis of the MnO^- fragments indicates that HVF slightly increases the thickness of the CEI film. In contrast, no significant shifts in peak positions were observed for the LiF^-, CO_3^-, and CH_2OF^- fragments. Significantly, the MnF_2^- signal under HVF is predominantly concentrated in the inner layer of the CEI, suggesting that, Mn^{2+} preferentially leaches from the bulk phase and reacts with F^- in the electrolyte to form fluorinated products. The minor discrepancies in MnF_2^- may be attributed to the insufficient high-voltage stability of the electrolyte/salt, which undergoes oxidative decomposition under HVF, releasing H^+ ions. This

leads to the generation of HF, which further induces the dissolution of Mn^{2+} from the material surface. Furthermore, the higher ARR under the HVF system may exacerbate the nucleophilic attack of surface O^{n-} species, thereby triggering a synergistic degradation of the cathode material through O-loss and Mn^{2+} dissolution. As illustrated in Figure 6b, the 3D reconstruction reveals a weak MnO^- signal at the surface after the HVF, indicating the formation of a thicker CEI film at the surface. In comparison to LVF, the LiF^-, CO_3^-, and CH_2OF^- signals are distributed throughout the CEI film after HVF, with a slightly enhanced intensity in the inner layer. This suggests that HVF exacerbates the decomposition of $LiPF_6$ and carbonate solvents. Furthermore, the 3D reconstruction of MnF_2^- after HVF reveals slightly stronger signals in the surface layer, indicating that high voltage induces more severe decomposition of $LiPF_6$, leading to the increase of HF.

Given that the bulk and interface often evolve in a coupled manner during cycling, we have conducted additional comparative analysis of the CEI structures after long-term cycling. As shown in Figure S14a, the samples after long cycles of LVF and HVF show almost the same CEI thickness, suggesting that the capacity degradation under HVF is not dominated by the interface. Nevertheless, the LVF samples exhibit an ordered double-layer CEI structure: the outer layer is mainly composed of inorganic products such as PO_3^- and LiF^-, while the inner layer consists of organic decomposition products including CH_2OF^- and CO_3^-. In contrast, the HVF samples display a disordered distribution of both inorganic and organic products in the outer layer (e.g., PO_3^-, LiF^-, and CH_2OF^-), with the inner layer comprising organic products (CO_3^-). This indicates that the ordered CEI structure under LVF is conducive to enhancing interface stability. The 3D reconstruction (Figure S14b) further reveals that LiF^- after long cycles of LVF is primarily distributed in the surface region, indicating the formation of a thicker and more rigid inorganic layer. In comparison, under HVF conditions, species such as LiF^-, CH_2OF^-, and CO_3^- are distributed throughout the entire CEI layer, with an intensified signals near the surface, suggesting continuous decomposition of electrolyte salts and solvents occurs over the cycling process. Notably, the 3D reconstruction of MnF_2^- after HVF reveals a slightly more intense signal at the surface, suggesting enhanced decomposition of $LiPF_6$ and increased release of Mn^{2+}, thereby leading to the accumulation of MnF_{2-}. Given that Mn^{2+} dissolution is primarily associated with out-of-plane TM migration and O-loss, this observation further indicates that structural distortion within the bulk phase also affects interfacial stability. However, compared to its impact on the structure, the influence of HVF on the surface/interface is relatively minor. The primary cause of capacity decay during cycling under the HVF protocol is the structural degradation of the cathode.

Conclusion

In conclusion, through multiscale characterization and mechanistic analysis, we systematically reveal the regulatory mechanism of the "capacity versus stability" trade-off in lithium-rich layered oxide (LRLO) cathodes under high-voltage formation (HVF, 4.65~4.8 V) condition. Specifically, HVF promotes the Li^+ deintercalation from the transition metal (TM) layer, triggering an increase in TM layer vacancies that catalyze in-plane TM migration. This migration drives an irreversible transformation in the OM_6 (M, cation) configuration from O4 (OLi_xTM_2) to O5 (OLi_yTM_1). This structural evolution enhances TM─O covalency and ligand–metal charge transfer (LMCT), thereby synergistically enhancing the anionic/cationic redox activity and achieving a 21.6% increase in initial capacity. Crucially, in spite of cycling at the same moderate voltage region (2.5~4.5 V) during subsequent cycle after HVF and LVF (the low-voltage formation, 4.5~4.55 V) conditions, respectively, the aggravated in-plane TM migration further aggravates out-of-plane TM migration after HVF step, leading to progressive structural degradation that manifests as a 15.8% decrease in capacity retention after 200 cycles. Compared with the LVF protocol, these successive structural degradations exacerbated under HVF are identified as the primary cause of the rapid decline in capacity retention.

The HVF protocol inherently sacrifices structural stability for capacity enhancement, which is an intrinsic limitation for the practical application of LRLO cathode. Critically, long-cycle degradation stems not from interface instability during initial HVF cycle, but from bulk structural evolution triggered by in-plane TM migration (the transformation of the OM_6 coordination configuration) and aggravated out-of-plane Li/Ni disordering. On the aspect of industrialization and battery companies, the cathode department needs to optimize this inherent defect of LRLO. At the same time, the electrolyte department is suggested to make efforts to inhibit the Mn^{2+} dissolution and the nucleophilic attack of oxidized lattice oxygen (O^{n-}) to mitigate interface side reactions, thereby enhancing the reversibility of O^{n-} and synergistically improves full-cell performance. Moreover, we also propose several modified approaches: a) optimizing the formation voltage to 4.55–4.6 V achieves an optimal balance between capacity (>195 mAh g^{-1}) and stability (200-cycle retention > 86%); b) implementing cation gradient doping enhances the migration barriers for TM ions in both the in-plane and out-of-plan directions;[48] c) applying anti-nucleophilic attack electrolyte engineering (e.g., fluorinated electrolytes) and/or pulse activation strategies[49,50] to suppress the nucleophilic reaction of O^{n-} and mitigates interface side reactions. From the fundamental research perspective, this study offers a comprehensive analysis of the critical issues highlighted by the lithium battery industry, develops a structural evolution model and verifies its underlying mechanisms, providing a clear framework to guide future modification strategies.

Acknowledgements

This work was partially supported by the Natural Science Foundation of China (grant no. 92472203, 22288102 and 22021001). This research also employed the resources of the Shanghai Synchrotron Radiation Facility of BL11B and

BL02B02 beamline stations (https://cstr.cn/31124.02.SSRF.BL11B, https://cstr.cn/31124.02.SSRF.BL02B02). The authors appreciate the RIXS characterization (proposal-Info: 232–12226-ST) at beamline U41-PEAXIS of Bessy II, Helmholtz-Zentrum Berlin für Materialien und Energie (HZB), Berlin, Germany.

Open access funding enabled and organized by Projekt DEAL.

Conflict of Interests

The authors declare no conflict of interest.

Data Availability Statement

The data that support the findings of this study are available from the corresponding author upon reasonable request.

Keywords: Anionic redox · Formation voltage · Lithium-ion batteries · Lithium-rich layered oxide cathode · TM migration

[1] Y. Yang, W. Yang, H. Yang, H. Zhou, *eScience* **2023**, *3*, 100170.
[2] Y. Tian, C. Lin, X. Meng, X. Yu, H. Li, R. Xiong, *eScience* **2025**, *5*, 100325.
[3] Z. Xiao, J. Meng, Q. Li, X. Wang, M. Huang, Z. Liu, C. Han, L. Mai, *Sci Bull (Beijing)* **2018**, *63*, 46–53.
[4] Q. Li, D. Zhou, L. Zhang, D. Ning, Z. Chen, Z. Xu, R. Gao, X. Liu, D. Xie, G. Schumacher, X. Liu, *Adv. Funct. Mater.* **2019**, *29*, 1806706.
[5] X. Wu, X. Lou, C. Hu, F. Geng, J. Li, C. Li, B. Hu, *ACS Energy Lett.* **2024**, *10*, 459–468.
[6] E. Wang, Y. Zhao, D. Xiao, X. Zhang, T. Wu, B. Wang, M. Zubair, Y. Li, X. Sun, H. Yu, *Adv. Mater.* **2020**, *32*, 1906070.
[7] X. Cao, H. Li, Y. Qiao, M. Jia, H. Kitaura, J. Zhang, P. He, J. Cabana, H. Zhou, *Sci Bull (Beijing)* **2022**, *67*, 381–388.
[8] Y. Li, Z. Shi, B. Qiu, J. Zhao, X. Li, Y. Zhang, T. Li, Q. Gu, J. Gao, Z. Liu, *Adv. Funct. Mater.* **2023**, *33*, 2302236.
[9] X. Xu, S. Chu, S. Xu, S. Guo, H. Zhou, *Energy Environ. Sci.* **2024**, *17*, 3052–3059.
[10] S. Zhang, Z. Yang, Y. Lu, W. Xie, Z. Yan, J. Chen, *Adv. Energy Mater.* **2024**, *14*, 2402068.
[11] D. Eum, B. Kim, S. J. Kim, H. Park, J. Wu, S. Cho, G. Yoon, M. H. Lee, S. Jung, W. Yang, W. M. Seong, K. Ku, O. Tamwattana, S. K. Park, I. Hwang, K. Kang, *Nat. Mater.* **2020**, *19*, 419–427.
[12] D. Seo, J. Lee, A. Urban, R. Malik, S. Kang, G. Ceder, *Nat. Chem.* **2016**, *8*, 692–697.
[13] Y. Liu, D. Ning, L. Zheng, Q. Zhang, L. Gu, R. Gao, J. Zhang, A. Franz, G. Schumacher, X. Liu, *J. Power Sources* **2018**, *375*, 1–10.
[14] L. Zeng, H. Liang, B. Qiu, Z. Shi, S. Cheng, K. Shi, Q. Liu, Z. Liu, *Adv. Funct. Mater.* **2023**, *33*, 2213260.
[15] Y. Yang, J. Cai, Y. Zuo, K. Zhang, C. Gao, L. Zhou, Z. Chen, W. Chu, D. Xia, *Energy Storage Mater.* **2024**, *71*, 103587.
[16] J. Song, F. Ning, Y. Zuo, A. Li, H. Wang, K. Zhang, T. Yang, Y. Yang, C. Gao, W. Xiao, Z. Jiang, T. Chen, G. Feng, D. Xia, *Adv. Mater.* **2023**, *35*, 2208726.
[17] E. Wang, D. Xiao, T. Wu, X. Liu, Y. Zhou, B. Wang, T. Lin, X. Zhang, H. Yu, *Adv. Funct. Mater.* **2022**, *32*, 2201744.
[18] J. Li, J. Tang, J. Tian, C. Cheng, Y. Liao, B. Hu, T. Yu, H. Li, Z. Liu, Y. Rao, Y. Deng, L. Zhang, X. Zhang, S. Guo, H. Zhou, *J. Am. Chem. Soc.* **2024**, *146*, 7274–7287.
[19] B. Li, K. Zhang, Y. Yang, Y. Zuo, X. Li, D. Xia, *Adv. Mater.* **2024**, *36*, 2400259.
[20] G. Assat, D. Foix, C. Delacourt, A. Iadecola, R. Dedryvère, J. Tarascon, *Nat. Commun.* **2017**, *8*, 2219.
[21] K. Zhang, Y. Chen, Y. Zhu, Q. Zheng, Y. Tang, D. Yu, Q. Liu, H. Luo, J. Yin, L. Zeng, W. Jiao, N. Liu, Q. Wang, L. Zheng, J. Zhang, Y. Wang, B. Zhang, Y. Yan, H. Huang, C. Shen, Y. Qiao, S. Sun, *Angew. Chem. Int. Ed.* **2025**, *64*, e202419909.
[22] B. Zhang, Y. Zhang, X. Wang, H. Liu, Y. Yan, S. Zhou, Y. Tang, G. Zeng, X. Wu, H. Liao, Y. Qiu, H. Huang, L. Zheng, J. Xu, W. Yin, Z. Huang, Y. Xiao, Q. Xie, D. Peng, C. Li, Y. Qiao, S. Sun, *J. Am. Chem. Soc.* **2023**, *145*, 8700–8713.
[23] Y. Li, W. Li, R. Shimizu, D. Cheng, H. Nguyen, J. Paulsen, S. Kumakura, M. Zhang, Y. S. Meng, *Adv. Energy Mater.* **2022**, *12*, 2103033.
[24] A. Ito, Y. Sato, T. Sanada, M. Hatano, H. Horie, Y. Ohsawa, *J. Power Sources* **2011**, *196*, 6828–6834.
[25] Y. Niu, Z. Hu, H. Mao, L. Zhou, L. Wang, X. Lou, B. Zhang, D. Xiao, Y. Yang, F. Ding, X. Rong, J. Xu, W. Yin, N. Zhang, Z. Li, Y. Lu, B. Hu, J. Lu, J. Li, Y. Hu, *Energy Environ. Sci.* **2024**, *17*, 7958–7968.
[26] L. Wang, A. Dai, W. Xu, S. Lee, W. Cha, R. Harder, T. Liu, Y. Ren, G. Yin, P. Zuo, J. Wang, J. Lu, J. Wang, *J. Am. Chem. Soc.* **2020**, *142*, 14966–14973.
[27] TA Ono, T Noguchi, Y Inoue, M Kusunoki, T Matsushita, H Oyanagi, *Science* **1992**, *258*, 1335–1337.
[28] E. Hu, X. Yu, R. Lin, X. Bi, J. Lu, S. Bak, K. Nam, H. L. Xin, C. Jaye, D. A. Fischer, K. Amine, X. Yang, *Nat. Energy* **2018**, *3*, 690–698.
[29] B. Li, Z. Zhuo, L. Zhang, A. Iadecola, X. Gao, J. Guo, W. Yang, A. V. Morozov, A. M. Abakumov, J. Tarascon, *Nat. Mater.* **2023**, *22*, 1370–1379.
[30] B. Li, M. T. Sougrati, G. Rousse, A. V. Morozov, R. Dedryvère, A. Iadecola, A. Senyshyn, L. Zhang, A. M. Abakumov, M. Doublet, J. Tarascon, *Nat. Chem.* **2021**, *13*, 1070–1080.
[31] X. Wu, Y. Jiang, X. Lou, Y. Liu, J. Li, J. Li, B. Hu, C. Li, *ACS Nano* **2024**, *18*, 20716–20725.
[32] C. Zheng, Y. Wang, H. Mao, J. Zhang, X. Yang, J. Li, D. Zhang, X. Wang, F. Kang, J. Li, *Nat. Commun.* **2025**, *16*, 3900.
[33] H. Zhang, J. Chen, Y. Hong, X. Wu, X. Huang, P. Dai, H. Luo, B. Zhang, Y. Qiao, S. Sun, *Nano Lett.* **2022**, *22*, 9972–9981, https://10.1021/acs.nanolett.2c03535.
[34] Z. Wu, G. Zeng, J. Yin, C. Chiang, Q. Zhang, B. Zhang, J. Chen, Y. Yan, Y. Tang, H. Zhang, S. Zhou, Q. Wang, X. Kuai, Y. Lin, L. Gu, Y. Qiao, S. Sun, *ACS Energy Lett.* **2023**, *8*, 4806–4817.
[35] J. Marie, R. A. House, G. J. Rees, A. W. Robertson, M. Jenkins, J. Chen, S. Agrestini, M. Garcia-Fernandez, K. Zhou, P. G. Bruce, *Nat. Mater.* **2024**, *23*, 818–825.
[36] X. Cao, Y. Qiao, M. Jia, P. He, H. Zhou, *Adv. Energy Mater.* **2022**, *12*, 2003972.
[37] Z. Zhuo, C. D. Pemmaraju, J. Vinson, C. Jia, B. Moritz, I. Lee, S. Sallies, Q. Li, J. Wu, K. Dai, Y. Chuang, Z. Hussain, F. Pan, T. P. Devereaux, W. Yang, *J. Phys. Chem. Lett.* **2018**, *9*, 6378–6384.
[38] R. A. House, U. Maitra, M. A. Pérez-Osorio, J. G. Lozano, L. Jin, J. W. Somerville, L. C. Duda, A. Nag, A. Walters, K. Zhou, M. R. Roberts, P. G. Bruce, *Nature* **2020**, *577*, 502–508.
[39] Q. Li, D. Ning, D. Wong, K. An, Y. Tang, D. Zhou, G. Schuck, Z. Chen, N. Zhang, X. Liu, *Nat. Commun.* **2022**, *13*, 1123.
[40] J. Zhang, Q. Zhang, D. Wong, N. Zhang, G. Ren, L. Gu, C. Schulz, L. He, Y. Yu, X. Liu, *Nat. Commun.* **2021**, *12*, 3071.
[41] A. Gao, X. Li, Q. Zhang, T. Lin, Y. Wang, Y. Chen, W. Lin, S. Wang, P. Ji, Z. Luo, J. Wang, Y. Guo, L. Gu, *Adv. Mater.* **2025**, *37*, 2412673.
[42] M. Kim, H. Jang, E. Lee, J. Seo, J. Park, A. Choi, T. Kim, M. Choi, E. Kim, Y. H. Jung, S. J. Kang, J. Cho, Y. Li, M. G. Kim, D. Seo, H. Lee, *Sci. Adv.* **2025**, *11*, eadt0232.

[43] L. Zeng, H. Liang, Y. Wang, X. Ying, B. Qiu, J. Pan, Y. Zhang, W. Wen, X. Wang, Q. Gu, J. Li, K. Shi, Y. Shen, Q. Liu, Z. Liu, *Energy Environ. Sci.* **2025**, *18*, 284–299.
[44] X. Li, Y. Zhang, B. Qiu, G. Chen, Y. Zhou, Q. Gu, Z. Liu, *Energy Environ. Mater.* **2024**, *0*, e12722.
[45] W. Liu, P. Oh, X. Liu, M. Lee, W. Cho, S. Chae, Y. Kim, J. Cho, *Angew. Chem. Int. Ed.* **2015**, *54*, 4440–4457.
[46] X. Zhang, J. Zhao, G. Lee, Y. Liang, B. Wang, S. Liu, E. Wang, W. Yang, H. Yu, *Adv. Energy Mater.* **2023**, *13*, 2202929.
[47] C. Liu, A. Dolocan, Z. Cui, A. Manthiram, *J. Am. Chem. Soc.* **2025**, *147*, 6023–6036.
[48] T. Wu, X. Liu, X. Zhang, Y. Lu, B. Wang, Q. Deng, Y. Yang, E. Wang, Z. Lyu, Y. Li, Y. Wang, Y. Lyu, C. He, Y. Ren, G. Xu, X. Sun, K. Amine, H. Yu, *Adv. Mater.* **2020**, *33*, 2001358.
[49] C. Xu, P. Jing, P. Xia, Y. Jia, J. Peng, Q. He, Q. Liu, Z. Song, X. Zhang, F. Wu, X. Liu, K. Wu, Y. Zhang, W. Cai, *Energy Environ. Sci.* **2025**, *18*, 7060–7070.
[50] T. Holstun, T. P Mishra, L. Huang, H. Hau, S. Anand, X. Yang, C. Ophus, K. Bustillo, L. ma, S. Ehrlich, G. Ceder, *Adv. Mater.* **2025**, *37*, 2412871.

Manuscript received: July 18, 2025
Revised manuscript received: September 02, 2025
Manuscript accepted: September 08, 2025
Version of record online: September 16, 2025